https://doi.org/10.5194/essd-2026-18
Preprint. Discussion started: 27 March 2026

Open Access Earth System Science Data Discussions

Extreme Precipitation Events: A Comprehensive Catalog for Northern Chile (17.5 °S to 30.0 °S)

Felipe Matus[1], Marcia Paredes[1], Miguel Lagos-Zúñiga[2], Alex Garcés[1], Diego Pinto[1], Germán Aguilar[1], and Santiago Montserrat[1]

[1]Advanced Mining Technology Center (AMTC), Faculty of Physical and Mathematical Sciences, University of Chile, Chile
[2]Departamento de Obras Civiles, Universidad Técnica Federico Santa María, Chile.

Correspondence: Santiago Montserrat (santiago.montserrat@amtc.uchile.cl)

Abstract. This study presents a comprehensive catalog of the extreme seasonal rainfall events of northern Chile between 1979 and 2019. We analyzed its meteorological patterns across three latitudinal bands (17.5ºS–23.5ºS, 23.5ºS–27ºS, and 27ºS–30ºS) using daily precipitation and mean daily temperature from the CR2METv2.5 product, and vertically integrated water vapor transport (IVT) data from ERA5 reanalysis. These events were classified into three main precipitation categories: Stratiform, Coastal, and Andes Mountain. The Andes Mountain category was further subdivided into five subcategories based on IVT patterns and precipitation location: north Andes, south Andes, along Andes, Convergence, and Westerly IVT. The catalog includes meteorological descriptors for each seasonal extreme event, such as: date, precipitation category, maximum precipitation within the latitudinal band, average storm temperature, and average snowline elevation determined using empirical method and MODIS remote sensing imagery. Additionally, we included the IVT and spatial snowcover derived from MODIS images for each event. To test the applicability of this catalog, we characterized extreme events composite results for the Austral summer between 27ºS–30ºS (latitudinal band 3). Additionally, we contrasted our catalog to existing landslide inventory and estimated approximate debris flow volumes for the March 2015 Atacama event. These findings can enhance the understanding of extreme precipitation events in arid and semiarid zones in Chile and provide a valuable resource for storyline analysis and precipitation pattern identification.

The catalog can be accessed through the Zenodo platform at https://doi.org/10.5281/zenodo.14342936.

1 Introduction

In recent decades, the study of extreme weather events from central to northern Chile has received increasing focus (Rondanelli et al., 2019; Valenzuela and Garreaud, 2019; Garreaud et al., 2020), because of their consequences in society: interruption of water supply, floods, debris flows, infrastructure damage and even human fatalities (Valenzuela et al., 2022). The interaction of geographical features, such as the Andes mountains, and Chile's significant latitudinal extent from tropics (∼17°S) to Patagonia (∼57°S), with dynamical features of climate ,such as the Southeast Pacific semi-permanent subtropical anticyclone, the synoptic scale disturbances from the westerly wind belt, and the South American-like monsoon system (SAMS), results in

https://doi.org/10.5194/essd-2026-18
Preprint. Discussion started: 27 March 2026

Open Access Earth System Science Data Discussions

a north-south (and east-west) mean precipitation gradient. Annual mean precipitation can vary from approximately 10 mm in the hyper-arid north to over 3,000 mm in southern Chile (Aceituno et al., 2021).

Precipitation in the arid northern region (above 30°S) mainly occurs during the austral summer (December to February), mostly related to convective systems (linked to SAMS), cut-off lows, and the presence of atmospheric rivers (Aceituno et al., 2021; Fuenzalida et al., 2005; Valenzuela and Garreaud, 2019; Rondanelli, 2025). The impact of these precipitation mechanisms on natural hazards is strongly modulated by the geomorphological configuration of northern Chile.

Northern Chile features a diverse geomorphological landscape comprising five distinct morphological domains: the Coastal Plain, the Coastal Range, the Intermediate Depression, the Precordillera, and the Andes Mountain Range (Börgel, 1983). Areas of high relief, particularly in the Andean Precordillera and valleys, are prone to debris flows triggered by extreme storms (Wilcox et al., 2016). Human settlements in these regions are often situated on alluvial fans, increasing their exposure to debris flow risks. Consequently, estimating sediment volumes that may reach inhabited alluvial fans is critical for hazard mitigation (Zegers et al., 2020; Garcés et al., 2022).

The magnitude and continuity of sediment transport to alluvial fans are strongly controlled by the hydrological and geomorphological setting of northern Chile. Rivers originating from the high Andean ranges are fed by snow and local aquifers, while glaciers and rock glaciers play an important role in maintaining the baseflow during low-precipitation periods (McPhee et al., 2021). These rivers flow through the Intermediate Depression, while the tributary ravines mainly feature ephemeral streamflow. The mountainous landscape in northern Chile is characterized by abundant sediments accumulating in alluvial, colluvial, and fluvial deposits. Most ravines in this region exhibit a condition of unlimited sediment availability, meaning that the sediment present in the basin exceeds the transport capacity during a flood event (Montserrat et al., 2025). This condition is typically found in ravines ranging from 0.1 to 30 km^2, although very steep ravines or those with substantial bedrock presence may not follow this pattern (Aguilar et al., 2020).

While sediment availability and channel connectivity define the preconditioning of these systems, extreme precipitation events act as the primary trigger for sediment mobilization and debris flows. Furthermore, the occurrence of precipitation recharges the groundwater systems. Depending on the intensity of the events and their warm conditions, they have triggered numerous catastrophic events (Bozkurt et al., 2016, e.g.,). Recent studies have explored the mechanisms behind water vapor sources to induce precipitation, as dry dynamics alone cannot account for the severity of extreme events (Rondanelli et al., 2019; Veloso, 2020; Rutllant et al., 2023, e.g.,). For example, Ortega et al. (2019) showed that since the beginning of the 20th century, about 70% of alluvial disasters in southern Atacama (26°-30°S) were related to the El Niño Southern Oscillation (ENSO) and the Pacific South America teleconnection pattern (PSA; Mo and Higgins, 1998).

One significant and recent historical weather event is the Atacama flood of 2015, caused by a two-day heavy rain that affected northern and central Chile, resulting in flash floods and debris flows (Wilcox et al., 2016; Bozkurt et al., 2016). Integrated analysis of this event highlights the key roles of ENSO and the Madden-Julian Oscillation (MJO) in the increased water vapor availability and its modulating transport mechanisms (Bozkurt et al., 2016; Rondanelli et al., 2019; Matus et al., 2025b). Rutllant et al. (2023) shows that in north-central Chile, rainfall-induced debris flows are related to high-amplitude

https://doi.org/10.5194/essd-2026-18
Preprint. Discussion started: 27 March 2026

Open Access Earth System Science Data Discussions

deep troughs extending into the subtropics off the west coast of South America and maximum integrated water vapor transport (IVT) from the northwest or west-northwest.

The snowline elevation, defined as the elevation where precipitation starts falling as snow - often related to the freezing level-, is another factor that can increase the possibility of hydro-meteorological hazards, such as floods and debris flow, as it determines the catchment contributing area to surface runoff generation (e.g. Valenzuela et al., 2022). Garreaud (2013) indicated that watersheds located in north and central Chile are the most affected during warm winter storms (north of 35°S), when the snowline elevation is high.

While considerable progress has been made in understanding extreme weather events in northern Chile, critical gaps still exist regarding the dominant mesoscale features and the areas they affect. In particular, the meteorological mechanisms driving extreme rainfall events in this region, which contribute to a complex and heterogeneous precipitation landscape, remain unclear. Despite the increasing focus on extreme climate events and their impacts, comprehensive records documenting and characterizing national extreme weather events are lacking. Key questions arise: What are the precise meteorological conditions that lead to extreme rainfall events in different latitudinal bands of northern Chile? How do integrated water vapor transport patterns contribute to these phenomena? Addressing these questions is crucial to reducing the knowledge gap and facilitating future studies on weather, the environment, and society.

This study aims to develop a catalog that analyzes and characterizes extreme precipitation events by season. These events have significant implications for the local population, posing risks of disasters such as floods and debris flows, as they represent the most severe weather conditions in the region. Documenting them contributes to meteorological and hydrological risk studies and enables practical applications such as composite analysis of storm dynamics, coarse estimation of debris flow volumes (based on precipitation-driven transport capacity), and characterization of rainfall-induced debris flow events. The catalog provides valuable insights into managing extreme precipitation events in northern Chile, particularly in sediment-rich, mountainous areas where rainfall intensity directly determines debris-flow magnitude. By linking storm characteristics to geomorphic impacts, this work bridges meteorological data with hazard assessment, supporting targeted risk mitigation strategies.

Section 2 outlines the study area, including its latitudinal bands, climate, and geographical context. Section 3 details the datasets and methodologies employed, emphasizing criteria for event selection and analytical frameworks for snow line elevation. Building on this foundation, Section 4 presents the catalog results an analysis of extreme precipitation events, identifying storm-dominant characteristics through maps and dynamical diagnostics. Section 5 demonstrates the catalog's applied potential, including composite storm analysis, contrast of rainfall-induced debris flow events, and coarse estimation of debris flow volumes illustrated through a case study of a debris flow triggered by an extreme rainfall event. Finally, Section 6 synthesizes key findings, provides discussions, and concludes our research.

https://doi.org/10.5194/essd-2026-18
Preprint. Discussion started: 27 March 2026

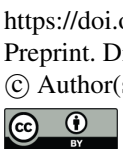

Open Access Earth System Science Data Discussions

2 Study Areas

To facilitate the isolation of precipitation events from different weather systems, the region is divided into three distinct areas according to latitude, the spatial distribution of precipitation climatology, and the frequency and intensity of precipitation events (as shown in (Aceituno et al., 2021)). These latitudinal bands, as shown in Figure 1, are defined as follows: (1) Latitudinal Band 1 (LB1, red) covers from 17.5ºS to 23.5ºS, (2) Latitudinal Band 2 (LB2, black) from 23.5ºS to 27ºS, and (3) Latitudinal Band 3 (LB3, green) from 27ºS to 30ºS. Moving forward, these bands will be referred to as LB1, LB2, and LB3.

Figure 1 further characterizes the study area, showing the elevation in northern Chile, reaching over 5.000 m a.s.l. and the composites of mean extreme precipitation events, from the catalog, for summer (DJF), fall (MAM), winter (JJA), and spring (SON) seasons. This climate feature displays the behavior of precipitation patterns among the strongest events within all latitudinal bands. During summer, most precipitation is concentrated in the Andes with moderate mean precipitation ($< 10mm/day$), while intermediate seasons show an NE to SW gradient of precipitation, with higher affected areas during fall. Finally, winter features the strongest precipitation events, which are mostly concentrated in LB3, reaching up to 20 mm/day on average.

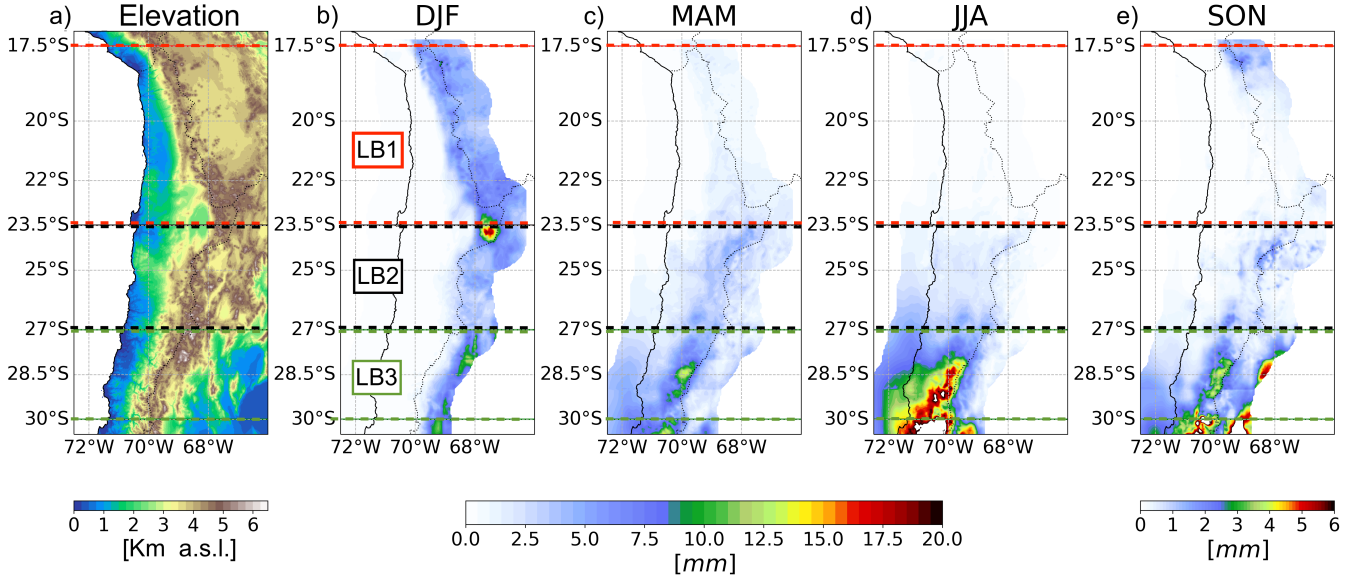

Figure 1. Climate and elevation features in northern Chile. The leftmost panel displays the topography (km); subsequent panels show the composite of maximum precipitation events (in mm) for each season along the three latitudinal bands (DJF: December–February, MAM: March–May, JJA: June–August, SON: September–November).

https://doi.org/10.5194/essd-2026-18
Preprint. Discussion started: 27 March 2026

Open Access Earth System Science Data Discussions

3 Data and Methods

We analyzed seasonal extreme precipitation events from 1979 to 2019, using the CR2METv2.5 precipitation product (Boisier et al., 2018). CR2Met is a station-based gridded product constructed using logistic regression for precipitation occurrence and multiple linear regression using topographic features and ERA5 fields for the same period. We also analyzed vertically integrated water vapor transport (IVT) derived from the ERA5 reanalysis (Hersbach et al., 2020), calculated between the surface (sfc) and the top of the atmosphere pressure levels (toa, equivalent to 0.01 hPa; equation 1). Precipitation data show daily accumulated values, and IVT was analyzed at 20 UTC (16:00 local time) to capture vapor transport characteristics during the typical afternoon period of enhanced convective activity (e.g., Falvey and Garreaud, 2005; Garreaud, 2009).

For each season, we identified the day with the maximum daily precipitation (grid cell level), hereafter referred to as the maximum seasonal precipitation event. We focused on these extreme values because they are more directly associated with severe impacts, such as floods and landslides, in contrast to averages over larger areas that may dilute the intensity of localized events. Maximum precipitation events were analyzed and classified across northern Chile within the three defined latitudinal bands (LBs). While all extreme precipitation events identified from 1979 to 2019 fall under defined main categories, not all subcategories appear in every season, and years with negligible or atypical events were excluded to focus on well-defined cases.

$$\overrightarrow{IVT} = -\frac{1}{g}\int_{sfc}^{toa} q\boldsymbol{V}\,dp \tag{1}$$

The snowline elevation was estimated for each event through the use of an empirical method, as well as remote sensing techniques in order to quantify the difference obtained from both methods. Equation 2, proposed by Garreaud (1992), estimates the snow line elevation as the freezing level (0°C, denoted as H_0) of the event minus 300 m; this elevation difference comes from the ratio between the moist lapse rate ($\sim \gamma = 5.8°C/km$) and the threshold temperature to discriminate between solid and liquid precipitation (∼1–2 °C) in Chile. The freezing level H_0 was estimated through a linear regression between the surface height and the mean temperature from the CR2MET product during each event, considering only the grid-cells affected by precipitation, as very different conditions may be observed at similar latitudes (see the DJF composite in Figure 1). For elevation, we upscaled the Shuttle Radar Topography Mission digital elevation model (Farr et al., 2007) to the CR2MET grid resolution (0.05°).

$$H_{SL}^{E} = H_0 - 300\ \text{m} \tag{2}$$

The snow line estimation through remote sensing used the MODIS Snow Cover daily product (MOD10A1 and MYD10A1, version 6.1) derived from the TERRA and AQUA satellites (Hall et al., 2002; Hall and Riggs, 2021a, b). We created a gridded binary time serie with a 500 m spatial resolution during 2000–2019, indicating snow/no snow based on each cell's normalized difference snow index (NDSI) value informed by MODIS Snow Cover. We considered those cells with a $NDSI \geq 0.4$ as snow (DeWalle and Rango, 2008), and the opposite case as no snow. Additionally, we estimated the presence of snow/no snow

https://doi.org/10.5194/essd-2026-18
Preprint. Discussion started: 27 March 2026

for the cloud-covered pixels (identified as no data by the satellites) for each day according to the methodology proposed by Gafurov and Bárdossy (2009): 1) merging TERRA and AQUA imagery for the same day, where cloud-covered pixels can be filled complementing both satellites, 2) a temporal fill, where missing pixels can be flagged as snow when the previous and/or the next day has snow, 3) an elevation fill, where cloud-covered pixels were filled as snow if their elevation is greater than the maximum snow elevation observed for day i, and not snow otherwise, and 4) neighbor comparison filling, according to the dominant snow presence in their neighborhood. After the gridded binary was complete, the observed snowline elevation by remote sensing (H_{SL}^{RS}) was calculated based on the methodology described by Krajčí et al. (2014): we determined the total number of snow pixels below each elevation in the latitudinal band (P_S) and the total number of no snow pixels above it (P_L); the snowline is then selected as the elevation H where $P_S + P_L$ is minimum (Equation 3). This optimization defaults to the maximum elevation in the latitudinal band when there is no snow cover, and the minimum elevation when the the whole area is covered.

$$H_{SL}^{RS} = H\left[\min(P_S + P_L)\right] \tag{3}$$

Figure 2 presents a flow chart illustrating the criteria and processes used to identify seasonal extreme precipitation events and determined their associated snowline elevations during the study period.

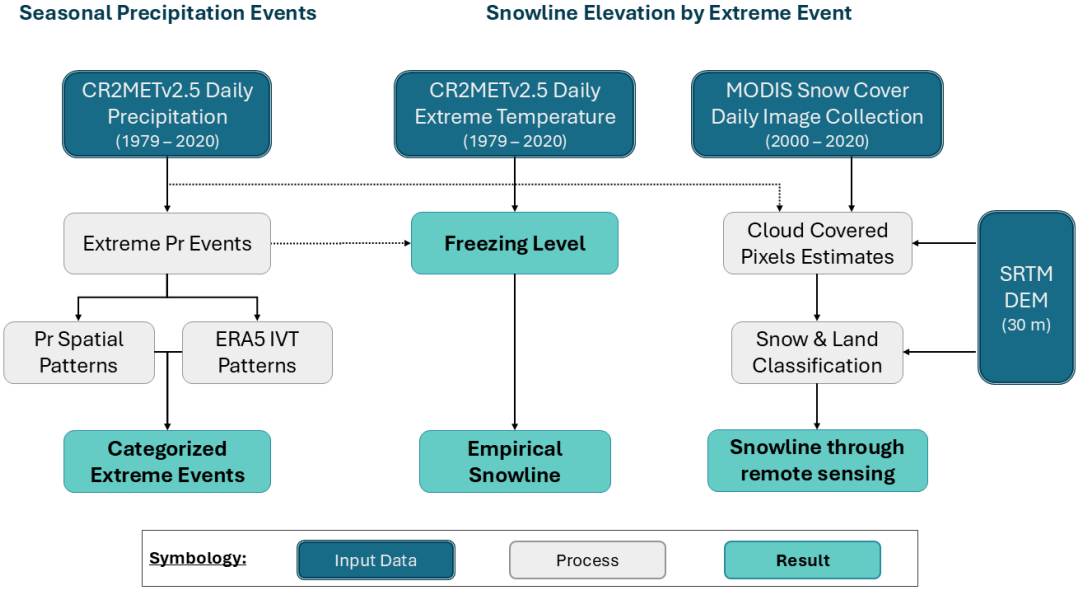

Figure 2. Flowchart of the process and selection of extreme precipitation events and the estimation of snowline elevation during the events. The methodology was applied for each latitudinal band from 1979 to 2019.

https://doi.org/10.5194/essd-2026-18
Preprint. Discussion started: 27 March 2026

Open Access Earth System Science Data Discussions

4 Results

4.1 Extreme precipitation events classification

To illustrate the diversity of spatial precipitation patterns from the catalog, Figure 3 shows examples of events from all latitudinal bands and seasons, highlighting the diversity of precipitation patterns identified in this study. These events represent the general precipitation categories for each latitudinal band: (1) $Andes\ Mountain$, with precipitation over the Andes (panels a, b, e, f); (2) $Stratiform$, with precipitation spread over most of the latitudinal band (panel c); and (3) $Coast$, with precipitation concentrated along and near the coastline (panel d).

https://doi.org/10.5194/essd-2026-18
Preprint. Discussion started: 27 March 2026

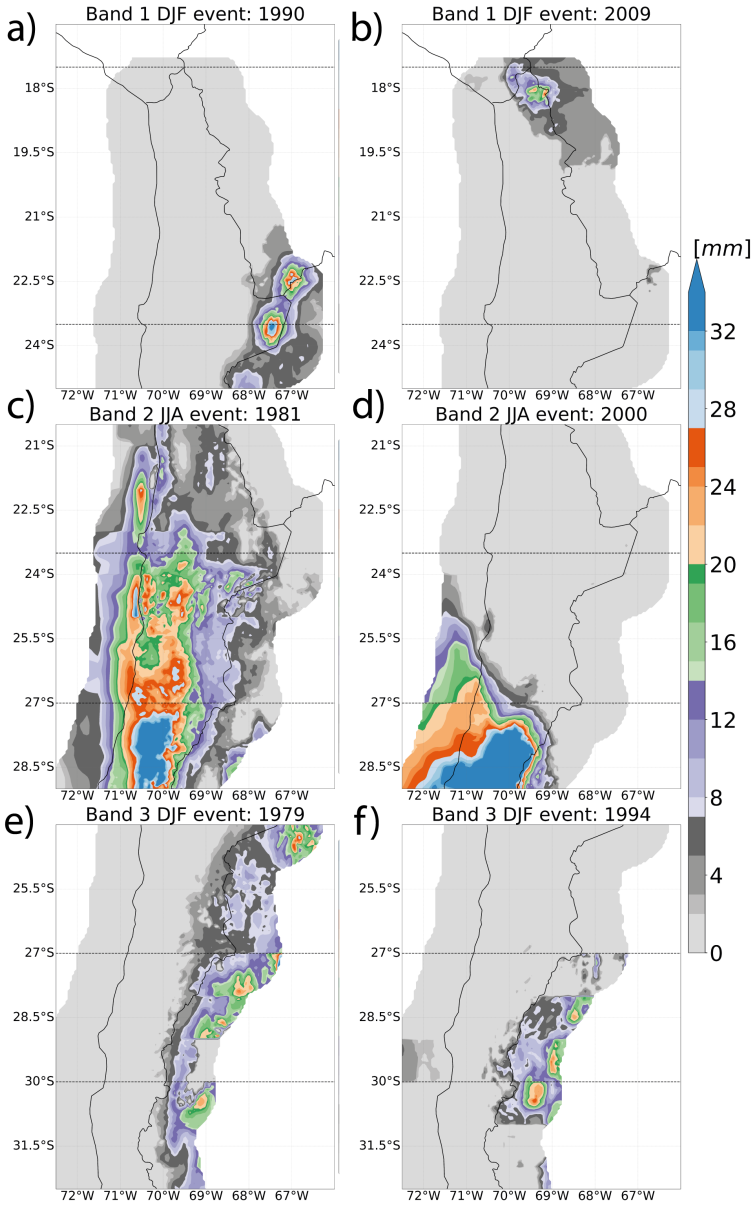

Figure 3. Examples of precipitation patterns (mm) for the extreme precipitation events identified in the catalog. The black rectangle delimits the latitudinal band related to the event. The panels a) and b) show the summer events of 1990 and 2009 in LB1, with a *Andes Mountain/South Andes* and *Andes Mountain/North Andes* category, respectively; panels c) and d) correspond to the winter events of 1981 and 2000 in LB2, with a *Stratiform* and *Coast* category, respectively; and the panels e) and f) are the summer events of 1979 and 1994 in LB3, with a *Andes Mountain/Along Andes* category.

We found that the *Andes Mountain* category can be further divided into subcategories based on precipitation location and associated water vapor transport, which vary across latitudinal bands and seasons. We identified three main subcategories based

https://doi.org/10.5194/essd-2026-18
Preprint. Discussion started: 27 March 2026

on the precipitation distribution along the mountain sector of the LBs: (1) $South\ Andes$, with precipitation concentrated in the southern sector (Figure 3a); (2) $North\ Andes$, with precipitation concentrated in the northern sector (Figure 3b); and (3) $Along\ Andes$, with precipitation observed across the Andes sectors (Figure 3e in the three bands, and Figure 3f in LB2).

Figure 4 shows the IVT patterns for the extreme precipitation events shown in Figure 3. We analyzed the relationship between precipitation patterns and the associated water vapor transport structures. For example, the precipitation categories $Coast$ and $Stratiform$ (Figures 3c,d and 4c,d) are associated with a northwesterly IVT signal, although their magnitudes are distributed differently across space. In contrast, events in the category $Andes\ Mountain$ (Figure 3a,b,e,f) with similar precipitation patterns can exhibit different IVT structures, as shown in Figures 3e,f and 4e,f, characterized by moderate southerly water vapor transport parallel to the Pacific coast, with some intrusion to the continent, but with differences in transport from the Argentinian western Andes.

By comparing $Andes\ Mountain$ precipitation and IVT patterns, we further divided the subcategory $Along\ Andes$. In the austral summer, LB3 was the only region where clear differences in IVT patterns were observed between $Along\ Andes$ events. As a result, we classified the IVT signals into two distinct patterns: $Convergence$ and $Westerly\ IVT$. The $Convergence$ pattern is associated with IVT convergence from the South Pacific and the east of the Andes Mountains (Figure 4e). In contrast, the $Westerly\ IVT$ pattern is characterized by transport from the South Pacific (Figure 4f).

https://doi.org/10.5194/essd-2026-18
Preprint. Discussion started: 27 March 2026

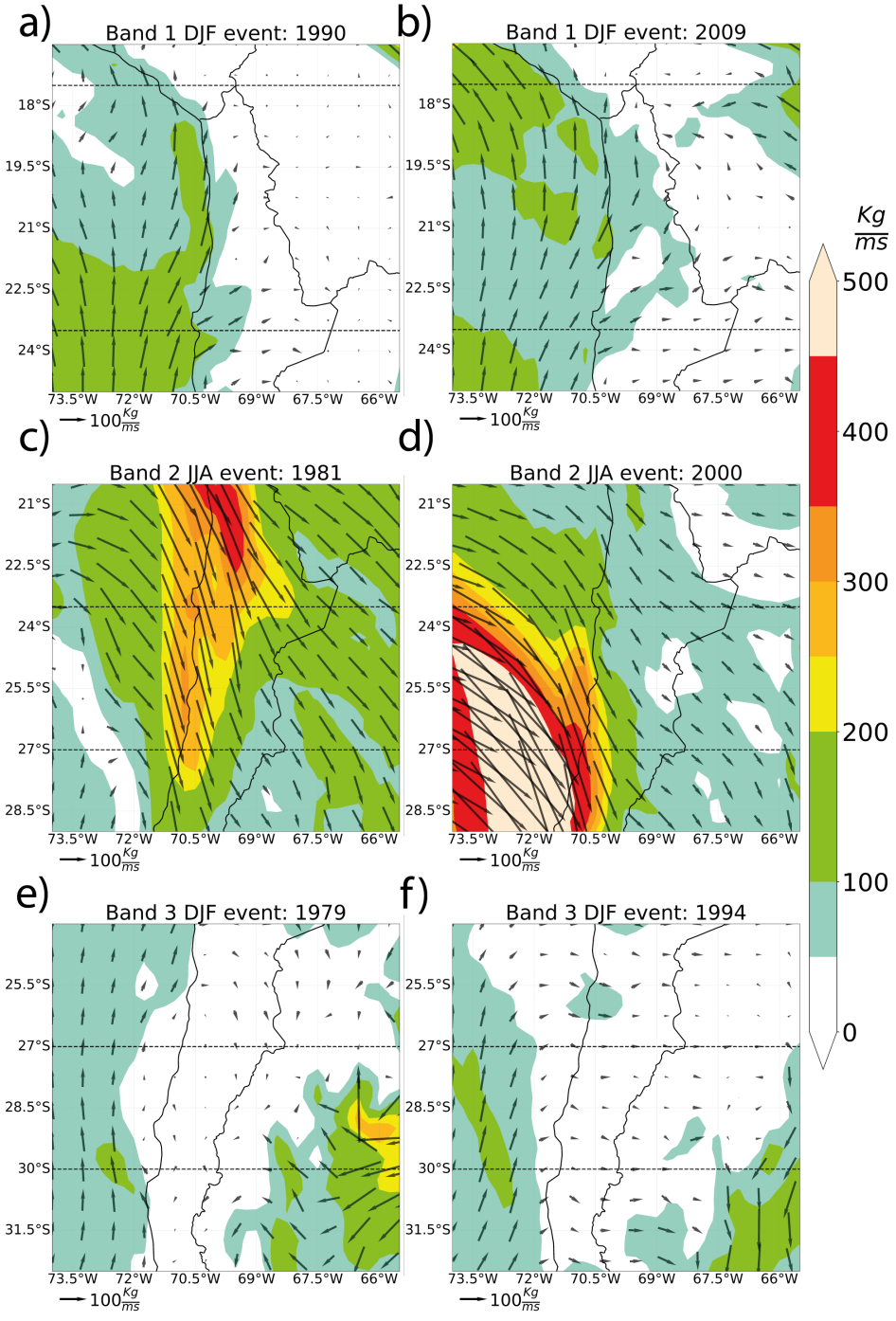

Figure 4. Examples of vertically Integrated Water Vapor Transport (kg/ms) patterns for the extreme precipitation events selected in the catalog. The black rectangle encloses the latitudinal band area related to the event. The uppermost panels show DJF LB1 results, the middle section corresponds to JJA LB2, and the lowermost panels are for DJF LB3 precipitation patterns.

https://doi.org/10.5194/essd-2026-18
Preprint. Discussion started: 27 March 2026

As a summary of our results, we identified three main categories of extreme precipitation events: $Andes\ Mountain$, $Coast$, and $Stratiform$. The category $Andes\ Mountain$ showed variability across events and was further divided into subcategories based on precipitation and IVT patterns: $North\ Andes$, $South\ Andes$, $Along\ Andes$, $Westerly\ IVT$, and $Convergence$.

To quantify the distribution of events and identify predominant patterns, Table 1 and Figures 5 provide a comprehensive overview. Table 1 summarizes the number of events per category, season, and latitudinal band, while Figures 5 illustrate the mean IVT directions for each category. Together, they offer insight into the spatial and seasonal distribution of extreme events and their associated IVT patterns.

Overall, not all categories are present in every season or latitudinal band, and some are more prevalent than others. As shown in Figure 5 (upper panel), most events in the catalog occur in the $Andes\ Mountain$, followed by $Stratiform$ events, which are primarily found in LB2 and LB3. It also illustrates the events distribution within the $Andes\ Mountain$ category, showing that $Along\ Andes$ events are the most frequent, particularly toward LB3 (Figure 5, bottom panel). While each category is generally associated with a characteristic IVT pattern, the subcategories $Convergence$ and $Westerly\ IVT$ are observed only in LB3 during the austral summer, reflecting the mixed distribution of IVT patterns in these events rather than a single dominant IVT type, and highlighting the seasonal and spatial specificity of these patterns.

Table 1. Number of events per category, season and latitudinal band of the catalog. The main category $Andes\ Mountain$ is shown separated as $North\ Andes$, $South\ Andes$, $Along\ Andes$, $Westerly\ IVT$, and $Convergence$.

Band	Category	Season			
		DJF	MAM	JJA	SON
LB1	North Andes	4	5	6	12
	Along Andes	32	27	10	19
	South Andes	5	9	10	0
	Stratiform	0	0	13	8
LB2	North Andes	18	0	0	9
	Along Andes	16	15	4	12
	South Andes	7	0	0	5
	Stratiform	0	26	30	15
	Coast	0	0	4	0
LB3	Westerly IVT	18	0	0	0
	Convergence	23	0	0	0
	Coast	0	3	4	8
	Stratiform	0	22	31	16
	Along Andes	0	14	4	8

https://doi.org/10.5194/essd-2026-18
Preprint. Discussion started: 27 March 2026

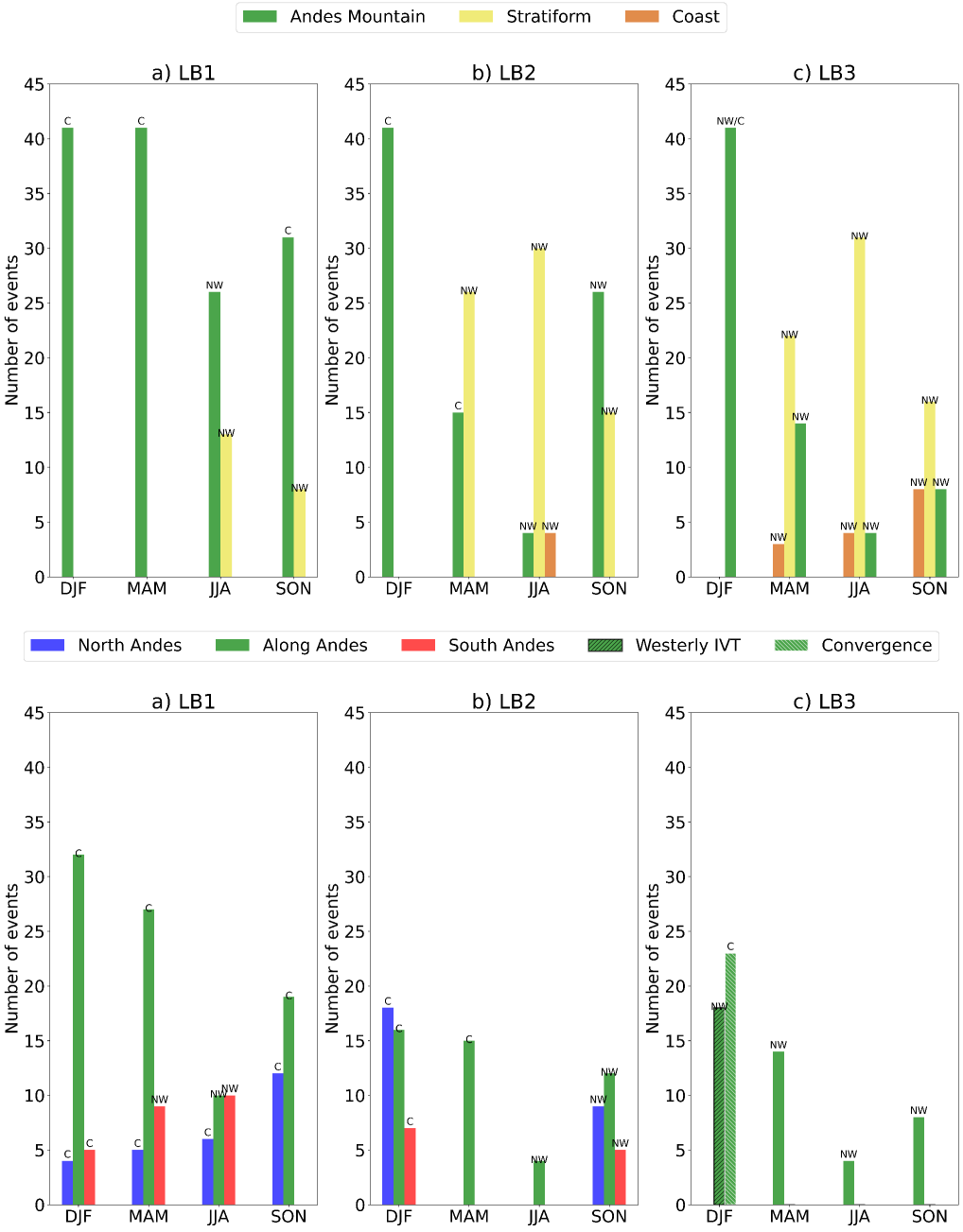

Figure 5. Bar plots for the number of events per category, season, and latitudinal band, observed in Table 1. The upper panel exhibit the distribution of events for the three main categories (*Andes Mountain*, *Stratiform*, and *Coast*). The bottom panel depicts the number of events per subdivision of the *Andes Mountain* category. 'NW' and 'C' correspond to *Northwesterly* and *Convergence*, which are the mean IVT directions observed in the composites of the categories by season over the latitudinal bands.

https://doi.org/10.5194/essd-2026-18
Preprint. Discussion started: 27 March 2026

Open Access Earth System Science Data Discussions

4.2 Freezing level and snowline delimitation

The observed snowline elevation derived from remote sensing during 2000–2019 exhibits different seasonal patterns across the latitudinal bands (Figure 6.A). In LB1, the median snowline elevation remains relatively constant throughout the seasons
185 regardless of storm category (4370 – 4462 m a.s.l., Figure 6.A.a); however, Stratiform events in this band display greater variability and slightly lower mean elevations compared to events occurring in the Andes Mountains (see Table 2).

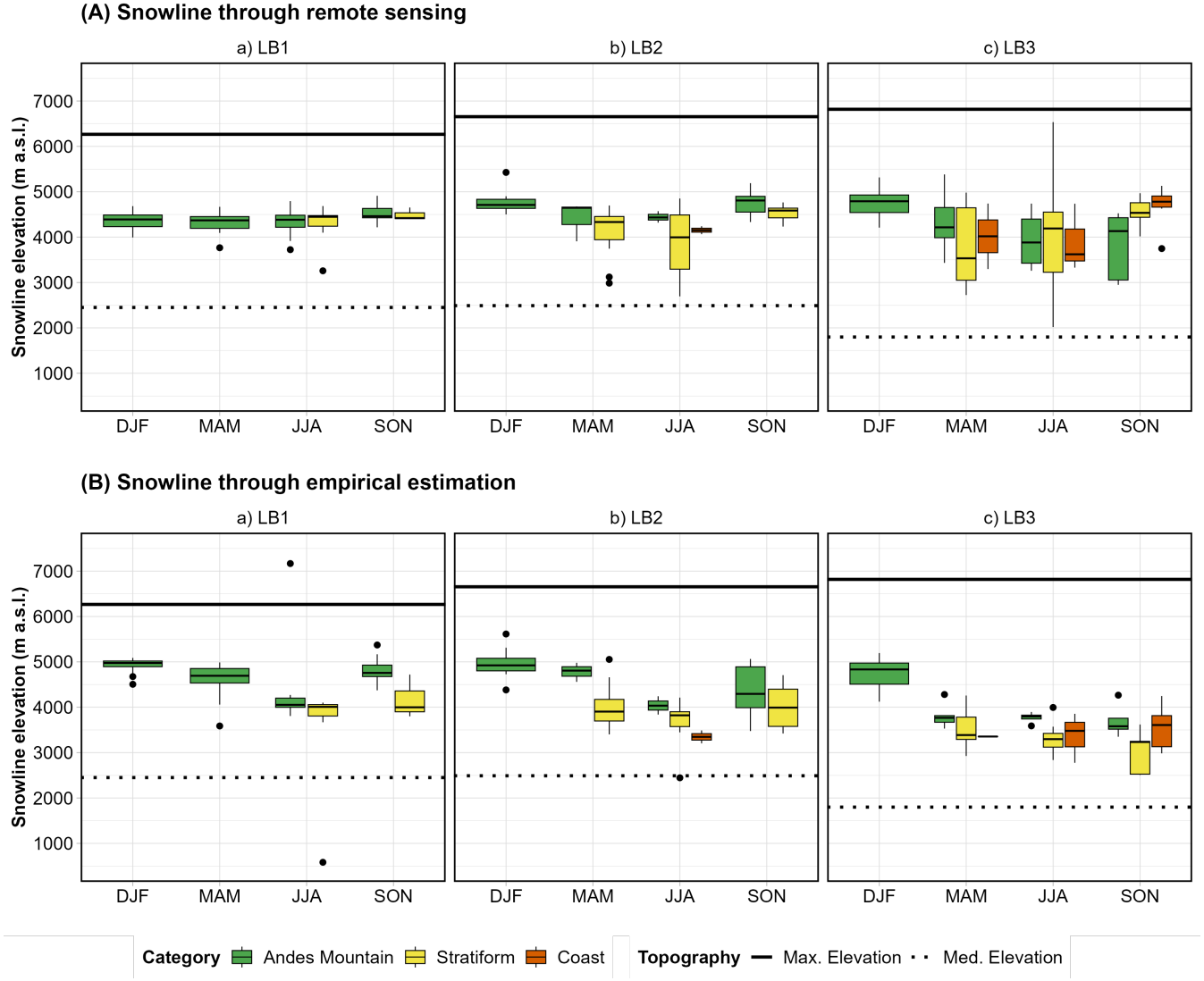

Figure 6. A) Snowline elevation detected through MODIS imagery, and B) estimated empirically in each latitudinal band, categorized by storm during 2000–2019. The Maximum (solid line) and median (dotted line) elevations by band are also included to illustrate the snow-covered area.

https://doi.org/10.5194/essd-2026-18
Preprint. Discussion started: 27 March 2026

In contrast, observed snowline elevations in LB2 and LB3 (Figure 6.A.b and 6.A.c) display a clear seasonal cycle that closely follows the regional air temperature and rainfall regime. Snowline elevations decrease during fall and winter, and reach their highest elevation during summer. In these bands, summer extreme precipitation events are primarily in the Andes Mountain category, with median snowlines of approximately 4750 m a.s.l. and standard deviation of 209 m in LB2 and 292 m in LB3. During colder seasons, Stratiform events in LB2 and LB3 typically show lower snowline elevations that those in the Andes Mountain and Coast categories, with differences of approximately 250 m in their mean values. The Coast category is observed only in LB2 and LB3 and shows higher snowline elevations than the Andes Mountain category during spring in LB3. Since Coast events are less frequent in the study area, its standard deviation is smaller compared to the other categories.

Empirical snowline elevations (Figure 6.B) are estimated using event-specific thermal gradients to determine the freezing level as a baseline for snowfall occurrence; this can result in estimates that may exceed the maximum elevation of the latitudinal band (see Figure 6.B.a, winter season). Unlike the remote sensing approach, the empirical method does not account for pre-existing snow cover, which represents a fundamental difference between the two methodologies. As shown in Figure 6.B.a, empirical snowlines for the Andes Mountain category are located, on average, 274 m higher than those derived from remote sensing, whereas lower elevations are obtained from the Stratiform events' thermic gradients. In LB2 and LB3, summer snowline estimates are similar in magnitude between methods, while the largest discrepancies between methods occur during spring, when empirical snowline elevations for the Stratiform and Coast categories are approximately 1062 m lower than those derived from remote sensing (Figure 6.A).

The main statistics for each method in the period 2000–2019 are presented in Table 2, where it can be seen that the empirical estimation tend to produce higher snowline estimations than remote sensing in LB1, and during austral summer and fall in LB2, however, to higher latitudes this method presented lower estimations around 200 m. These differences may have important consequences for extreme flows and landslide estimations, especially during years prior to 2000, where only empirical estimations could be made because of remote sensing data availability. Because of this, the use of empirical methods, including in-situ and upper-air observations, may help complement the analysis.

5 Catalog Applications

Extreme precipitation events in northern Chile have significant hydrometeorological and geomorphic impacts such as flood and debris flows. We explored how cataloged events can be used to identify synoptic-scale drivers of intense rainfall, assess the links between extreme storms and debris flows, and estimate potential sediment yields from high-impact rainfall events. By connecting precipitation patterns with geomorphic responses, these applications demonstrate the catalog's utility for hazard assessment and decision-making in regions prone to extreme rainfall and associated hazards.

5.1 Composites

We apply composite analysis to the different categories and latitudinal bands in order to explore the precipitation patterns and mechanisms of the registered extreme events. As a result, we capture the mean synoptic patterns associated with each

https://doi.org/10.5194/essd-2026-18
Preprint. Discussion started: 27 March 2026

Open Access Earth System Science Data Discussions

Table 2. Mean and standard deviation of the snowline estimated by both methods for each latitudinal band, season, and storm category for the extreme precipitations events during 2000–2019 and 1979–2019.

Band	Season	Storm category	Mean snowline through remote sensing (m a.s.l.)	Mean snowline through empirical estimation (m a.s.l.) Period: 2000 – 2019	Mean snowline through empirical estimation (m a.s.l.) Period: 1979 – 2019
LB1	DJF	Andes Mountain	4376 ± 201.5	4931 ± 144.8	4874 ± 186.4
	MAM	Andes Mountain	4327 ± 209.6	4633 ± 334.0	4637 ± 320.4
	JJA	Andes Mountain	4318 ± 283.7	4288 ± 877.0	3903 ± 1046.7
		Stratiform	4261 ± 475.1	3489 ± 1289.7	3630 ± 958.5
	SON	Andes Mountain	4526 ± 198.2	4792 ± 270.1	4787 ± 219.9
		Stratiform	4490 ± 141.2	4173 ± 484.1	4296 ± 395.7
LB2	DJF	Andes Mountain	4741 ± 209.4	4960 ± 256.6	4886 ± 233.9
	MAM	Andes Mountain	4410 ± 435.3	4782 ± 211.1	4742 ± 306.5
		Stratiform	4174 ± 500.3	3999 ± 431.1	4019 ± 357.7
	JJA	Andes Mountain	4442 ± 126.2	4039 ± 201.5	4005 ± 177.6
		Stratiform	3873 ± 714.1	3708 ± 451.6	3682 ± 379.8
		Coast	4153 ± 123.0	3347 ± 200.8	3296 ± 409.9
	SON	Andes Mountain	4745 ± 260.1	4392 ± 539.5	4317 ± 471.9
		Stratiform	4529 ± 189.2	4010 ± 493.4	3895 ± 416.5
LB3	DJF	Andes Mountain	4751 ± 291.7	4752 ± 326.0	4598 ± 453.2
	MAM	Andes Mountain	4330 ± 632.4	3793 ± 238.9	3913 ± 320.4
		Stratiform	3803 ± 837.7	3557 ± 416.5	3554 ± 496.1
		Coast	4018 ± 1020.4	3354 ± 0.7	3650 ± 512.4
	JJA	Andes Mountain	3941 ± 690.8	3770 ± 129.3	3770 ± 129.3
		Stratiform	4118 ± 1286.4	3280 ± 315.0	3289 ± 393.6
		Coast	3895 ± 742.7	3370 ± 547.8	3261 ± 497.6
	SON	Andes Mountain	3818 ± 759.7	3694 ± 351.3	3727 ± 358.1
		Stratiform	4543 ± 358.7	3027 ± 490.6	3460 ± 536.1
		Coast	4685 ± 444.7	3533 ± 479.2	3569 ± 455.1

event category. Here, we show the composite results for the LB3 austral summer *Convergence* category. Figure 7 exhibits precipitation over the Andes Cordillera. However, precipitation and standardized precipitation anomalies in LB3 are the highest. The three standard deviations from the mean observed in the LB3 indicate that the events selected to compose the catalog are

https://doi.org/10.5194/essd-2026-18
Preprint. Discussion started: 27 March 2026

Open Access Earth System Science Data Discussions

extreme events. Under normal distribution conditions, these events are related to probabilities of occurrence of less than 0.1% (∼10 years of return period, e.g. Rutllant et al., 2023).

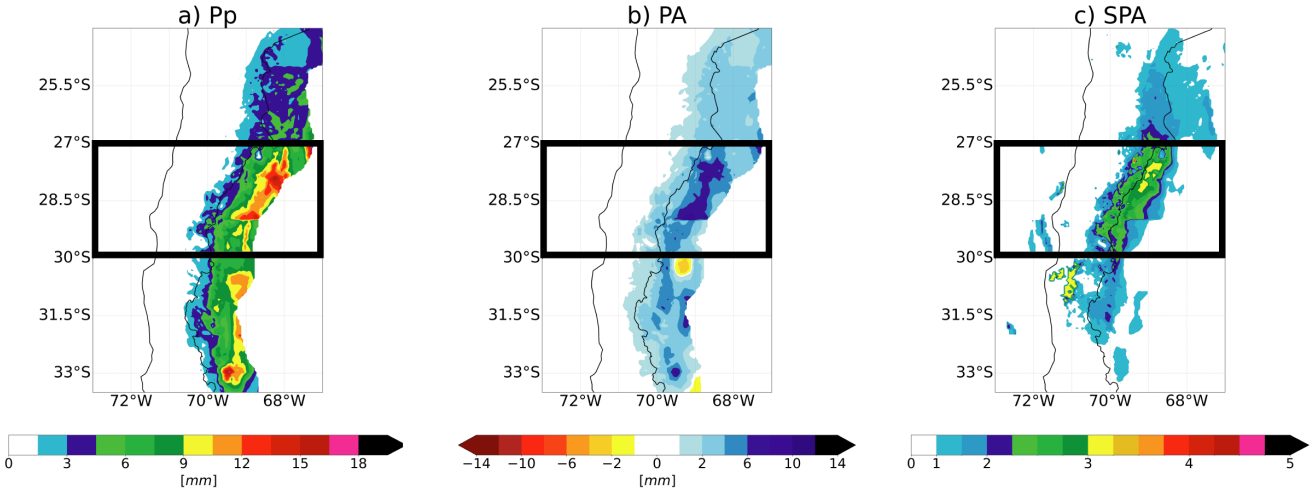

Figure 7. Composites for the LB3 *Convergence* category in austral summer (DJF) of: a) daily precipitation data (Pp), b) precipitation anomalies (PA, from daily climatology), and c) standardized precipitation anomalies (SPA, from daily climatology and daily standard deviation). The black rectangles frame the area related to the LB3 between 27°S–30°S.

These precipitation features are interpreted through the circulation patterns shown in the figure 8. We observe the presence of a ridge and anticyclonic circulation anomalies over southern South America and a trough with cyclonic circulation anomalies to the southwest of South America. Figure 9 shows the convergence of the IVT between the transport of water vapor from the Pacific and Argentina. The Pacific signal exhibits an anticyclonic circulation from the ridge-structured water vapor transport, with cyclonic deviation toward the LB3. The signal from Argentina displays anticyclonic circulation. Moreover, the anomaly and standardized anomaly analysis show that the IVT signal from Argentina has a higher standard deviation from the mean than the Pacific IVT, which is necessary to overpass the Andes.

https://doi.org/10.5194/essd-2026-18
Preprint. Discussion started: 27 March 2026

Open Access Earth System Science Data Discussions

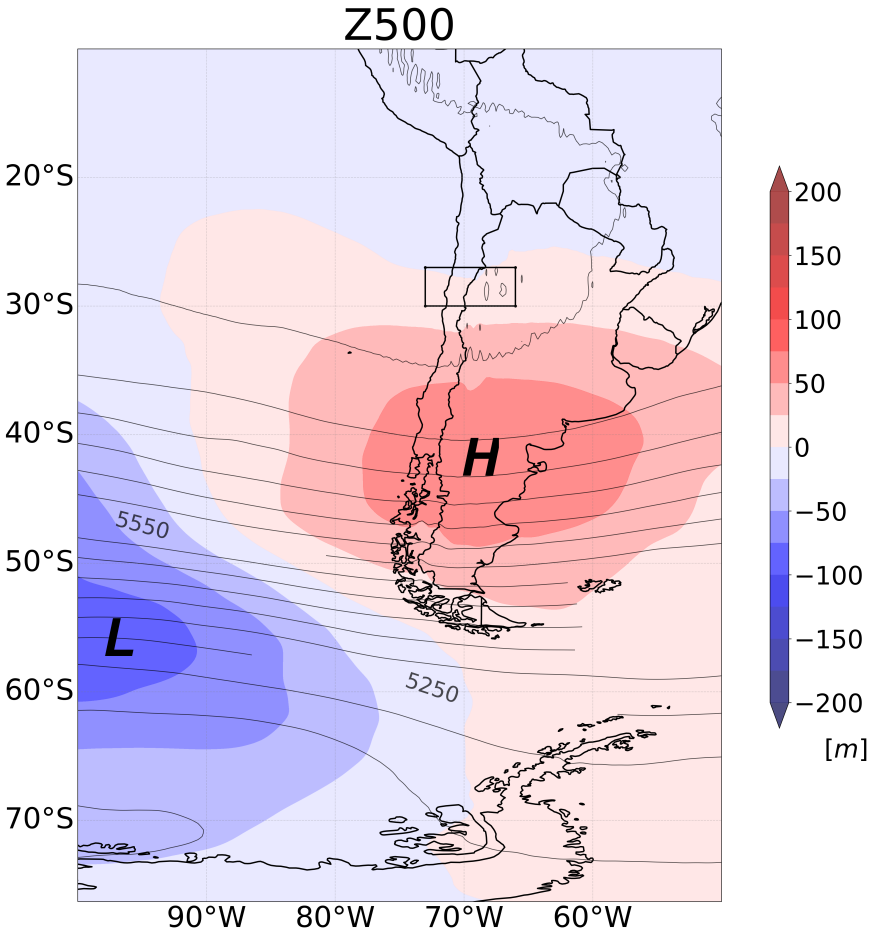

Figure 8. Composites of geopotential height at 500hPa (contours) and its anomalies (colors) for the category *Convergence* on austral summer (DJF). The black rectangle frames the area related to the LB3 between 27°-30°S. Cyclonic ("L") and anticyclonic ("H") circulation anomalies are highlighted.

https://doi.org/10.5194/essd-2026-18
Preprint. Discussion started: 27 March 2026

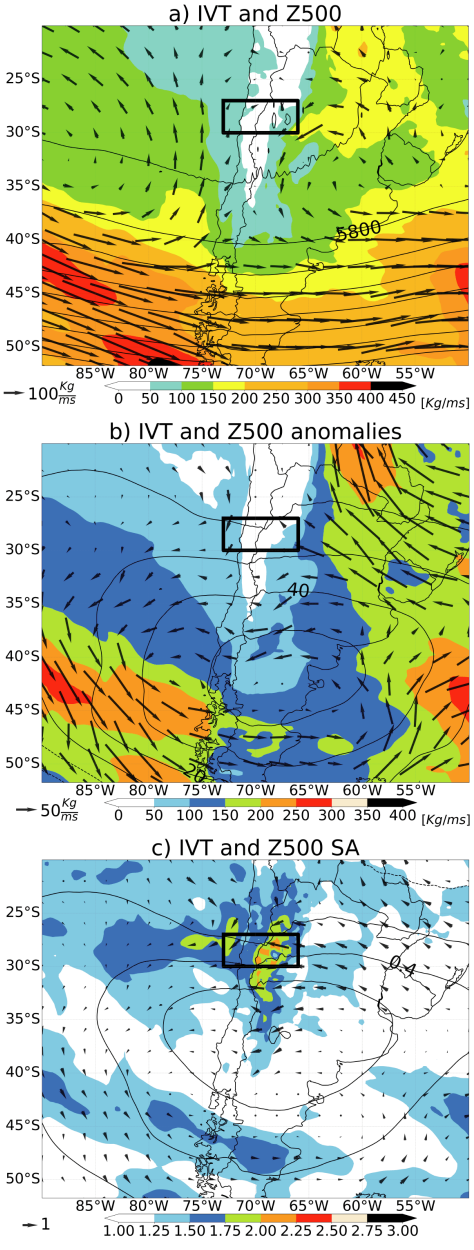

Figure 9. Austral summer (DJF) *Convergence* composites of Integrated water Vapor Transport (IVT; colors and vectors) and $Z500$ (contours) for (a) raw data, (b) anomalies, and (c) standardized anomalies (SA). The black rectangle frames the area related to the LB3 between 27°-30°S.

https://doi.org/10.5194/essd-2026-18
Preprint. Discussion started: 27 March 2026

5.2 Characterization of rainfall-induced mass movement events

The Chilean National Service for Geology and Mining (SERNAGEOMIN) compiled a mass movement inventory (available at https://www.plataformadedatos.cl/) reporting 1,046 debris flows and landslides caused by rain (excluding undated events), of which 548 (52.4%) occurred within the study area: 93 (8.9%) in LB1, 71 (6.8%) in LB2, and 384 (36.7%) in LB3. This highlights a significant presence of cataloged debris flow events in the study area. It is important to note that this inventory does not aim to document all events that have occurred. Instead, it focuses on events identified during periods of emergency or when an official threat was declared by authorities. Consequently, there is a gap between the events that actually occurred and those recorded in the inventory.

We contrasted the 548 events in the study area, finding that 203 (37%) are associated with six storms from the catalog (Table 3): one in LB1, three in LB2, and four in LB3 (two storms overlap Bands 2 and 3). All storms were stratiform. Most events occurred in Band 3 (170), particularly during two key storms in the MAM season: March 25, 2015 (97 events) and May 12, 2017 (71 events).

These findings show that this 6 storms in the catalog account for an important portion of the debris flow in the study area (37%), but not all. This discrepancy may be explained by the nature of rainfall-triggered debris flows, which result in either minor affected areas or in different intensities and durations that were not captured by the adopted criteria of our study (Berti et al., 2020; Zhang et al., 2020; Nikolopoulos et al., 2017). Short-duration, high-intensity events may not be identified as significant in the catalog because the analysis considers only the total daily precipitation of each event.

Table 3. Cataloged storms associated with debris flow and mass movement events per latitudinal band.

Band	Date	Season	Precipitation (mm)	Temperature (°C)	Freezing Level (m a.s.l.)	Observed Snowline Elevation (m a.s.l.)	# Events
LB1	09-08-2015	JJA	11.9	5.7	883	4489	11
LB2	16-05-2010	MAM	23.9	1.3	3819	4261	1
LB2	24-03-2015	MAM	61.4	10.5	4960	4333	11
LB2	12-05-2017	MAM	35.4	4.4	4014	4292	10
LB3	25-03-2015	MAM	45.3	10.1	4067	3044	97
LB3	12-05-2017	MAM	69.6	4.0	3687	2724	71
LB3	17-08-1997	JJA	111.5	2.1	3587		1
LB3	26-06-2017	JJA	43.1	4.2	3871	2806	1

5.3 Coarse estimation of debris flow volume

This application focuses on areas of high relief, which are prone to debris flows triggered by extreme storm events. Estimating the sediment volume that may reach inhabited alluvial fans is crucial, as human settlements in the Andean region are commonly situated on alluvial fans, making them vulnerable to debris flows (Romero et al., 2022; Garcés et al., 2022).

https://doi.org/10.5194/essd-2026-18
Preprint. Discussion started: 27 March 2026

Open Access Earth System Science Data Discussions

Research efforts have aimed to quantify erosion rates during extreme storm events (Aguilar et al., 2020) and over the long term (Aguilar et al., 2014). Aguilar et al. (2020) found that topographic attributes are the primary factor influencing the volumes of debris flows reaching the apex, with no significant correlation to lithological attributes. Their findings indicate that precipitation alone is sufficient to trigger debris flows since sediments are almost always available. Therefore, assuming unlimited sediment availability in the study area, the debris-flow volume produced by a storm event depends only on transport capacity. Consequently, coarse estimates of the debris-flow volume can be obtained from the catalog using a transport-capacity equation such as equation 4 (JICA, 2010).

$$V = 10^3 \; c \; Pp \; A \; \frac{1}{1-p} \left(\frac{C_d}{1-C_d} \right) \tag{4}$$

Where p is the porosity of the deposit, c is the runoff coefficient, Pp is the precipitation in mm, A is the area of the basin in km^2, and C_d is the sediment volumetric concentration, estimated using equation 5 (Takahashi, 2014).

$$C_d = \frac{\rho}{\rho_s - \rho} \frac{tan(\theta)}{tan(\phi) - tan(\theta)} \tag{5}$$

Where ρ_s is the density of the sediment, ρ the density of water, ϕ is the angle of internal friction of the sediment, and θ is the slope of the terrain.

Aguilar et al. (2020) surveyed debris–flow deposited volumes in 49 alluvial fans triggered by the 2015 storm event. Figure 10 compares these observed volumes with the transport capacity estimated for each basin based on the precipitation recorded in the event catalog. The estimated sediment transport capacity represents an upper bound on the volume that reaches the alluvial fan, as it does not account for processes that reduce delivery efficiency, such as sediment trapping or channel obstructions. Figure 10 indicates that this first–order estimation performs poorly for deposits smaller than 4000 m^3 ($pBIAS = 2053\%$), while the agreement between estimated and observed volumes improves markedly for deposits larger than this threshold ($pBIAS = 164\%$). The weak performance for small deposits likely reflects their higher sensitivity to measurement uncertainty, whereas larger deposits tend to reduce the relative error associated with field-based volume observation. Additionally, in some catchments, the systematic overestimation of deposited volumes may be influenced by sediment that was mobilized but ultimately bypassed the fan and continued downstream.

This model applies only to events in which prior knowledge of debris-flow occurrence exists, as the amount of rain is insufficient to trigger debris flows. The rainfall event must meet specific conditions not recorded in the catalog, such as rainfall intensity and/or duration. Hence, rainfall amounts in the catalog do not guarantee the occurrence of debris flow for that specific event.

6 Conclusions

Based on a comprehensive analysis of the selected maximum seasonal daily precipitation events across three latitudinal bands, we defined several storm categories that describe their main characteristics. These categories were created based on the ge-

https://doi.org/10.5194/essd-2026-18
Preprint. Discussion started: 27 March 2026

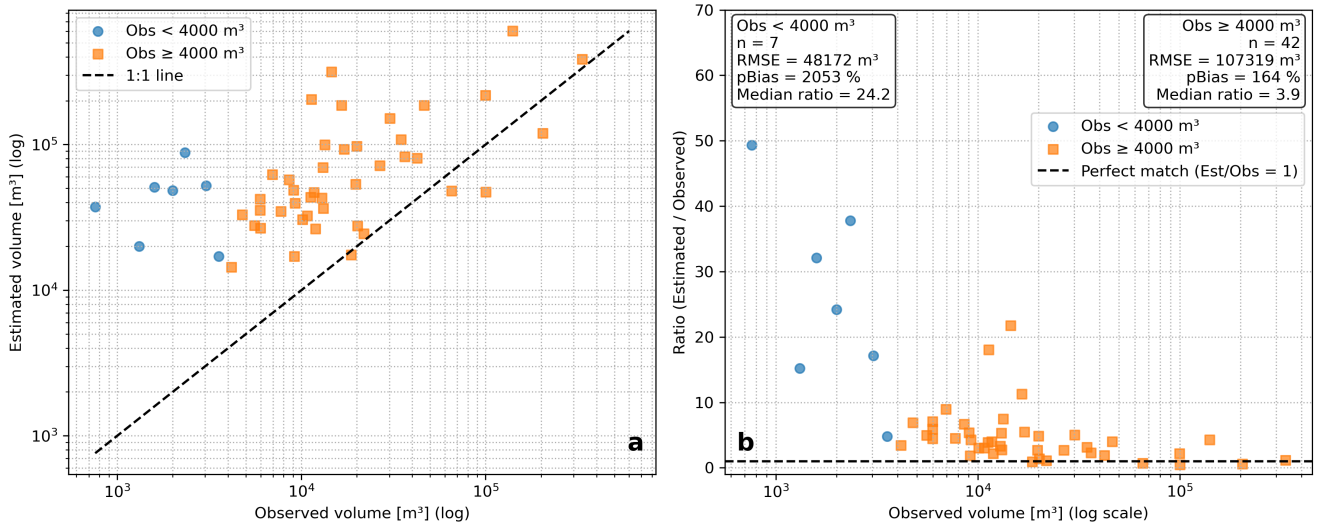

Figure 10. a) Coarse estimation of debris flow volume based on transport capacity for the March 2015 event. Comparison with measured deposited volumes at 49 alluvial fans. b) Ratio of estimated vs observed to quantify the prediction correlation degree

ographical region of precipitation and the pattern of water vapor transport they exhibit. On average, three distinct patterns for extreme events were found in each band and season, with the most common variations falling into the categories $Coast$, $Stratiform$, and $Andes\ Mountain$. In the category $Andes\ Mountain$, it was found that in certain seasons it could be further subdivided into $North\ Andes$, $South\ Andes$, and $Along\ Andes$ (along the Andes Cordillera), depending on the area of the mountain range where precipitation occurs.

Furthermore, we used the catalog and analyzed the composites for all the categories generated and, considering only the circulation and IVT, two general categories were identified encompassing all extreme events in different seasons and bands: (1) convergence of water vapor transport ($Convergence$); and (2) IVT from the Pacific ($Westerly\ IVT$). An exception arose in the $Along\ Andes$ pattern during summer in the LB3, where events exhibited a bimodal synoptic pattern. In this case, approximately half of the events were associated with $Convergence$ and the other half with $Westerly\ IVT$. Therefore, the $Along\ Andes$ category for this specific band and season was further subdivided into $Convergence$ and $Westerly\ IVT$ to represent the dual nature of the underlying mechanisms accurately.

As an example, the IVT convergence covers the results shown in Figure 9. It is also important to note that significant variations are observed between events classified into these two categories, including variability in the depth of development, circulation intensity, and IVT. These differences in atmospheric circulation and water vapor transport, combined with fluctuations in atmospheric moisture availability, contribute to the formation of a wide range of observed precipitation patterns. These factors also determine the extent to which these events can influence a specific latitudinal band.

https://doi.org/10.5194/essd-2026-18
Preprint. Discussion started: 27 March 2026

The catalog's utility extends beyond classification, enabling actionable insights for hazard management. First, composite analysis provides meteorological storylines—recurring synoptic scenarios like Convergence or Westerly IVT—that explain how extreme rainfall develops. These storylines are critical for early warning systems, as they link observable atmospheric patterns to high-impact precipitation. Second, the correlation of cataloged storms with 37% of historical debris flows (e.g., the March 2015 MAM event, which triggered 97 mass movements) underscores the catalog's value in identifying high-risk storms that disproportionately threaten Andean communities. Finally, the coarse estimation of debris-flow volumes via transport-capacity models (Figure 10) translates precipitation magnitudes into sediment-yield approximations, providing a first-order proxy for infrastructure planning and mitigation.

Together, these applications form a cohesive narrative: the catalog bridges atmospheric dynamics to geomorphic impacts, transforming theoretical classifications into practical frameworks for disaster risk reduction. By contextualizing extreme rainfall within both meteorological and societal contexts, this work advances preparedness in northern Chile's complex climatic and topographic setting.

7 Data availability

The catalog and the processed dataset (precipitation, IVT, and snowline elevations) are preserved in a Zenodo data repository with a corresponding assigned DOI, available at https://doi.org/10.5281/zenodo.14342936 (Matus et al., 2025a).

Author contributions. Felipe Matus, Marcia Paredes, Miguel Lagos-Zúñiga, and Santiago Montserrat designed the research methodology and the overall structure of the manuscript. Felipe Matus and Marcia Paredes prepared the initial draft of the manuscript and developed the catalog. Diego Pinto and Alex Garcés contributed to the applications presented in Sections 5.2 and 5.3. Felipe Matus and Miguel Lagos-Zúñiga proposed the event classification across the different bands and carried out the climatological analysis. Marcia Paredes processed the MODIS imagery and snowline elevations for each event. All authors contributed to the scientific discussion, and reviewed and approved the final version of the manuscript. Santiago Montserrat and Germán Aguilar led the funding project supporting this research (FONDEF ID22I10122, ANID).

Competing interests. The authors declare that they have no competing interests related to this catalog or its publication.

Acknowledgements. This research was funded by the Advanced Mining Technology Center (AMTC) via the basal projects AFB230001 ANID and CIA250010 ANID, and the project FONDEF ID22I10122 ANID.

https://doi.org/10.5194/essd-2026-18
Preprint. Discussion started: 27 March 2026

Open Access Earth System Science Data Discussions

References

Aceituno, P., Boisier, J. P., Garreaud, R., Rondanelli, R., and Rutllant, J. A.: Climate and Weather in Chile, 2021.

Aguilar, G., Carretier, S., Regard, V., Vassallo, R., Riquelme, R., and Martinod, J.: Grain size-dependent Be-10 concentrations in alluvial stream sediment of the Huasco Valley, a semi-arid Andes region, Quaternary Geochronology, 19, 163–172, https://doi.org/10.1016/j.quageo.2013.01.011, 2014.

Aguilar, G., Cabré, A., Fredes, V., and Villela, B.: Erosion after an extreme storm event in an arid fluvial system of the southern Atacama Desert: an assessment of the magnitude, return time, and conditioning factors of erosion and debris flow generation, Natural Hazards and Earth System Sciences, 20, 1247–1265, 2020.

Berti, M., Bernard, M., Gregoretti, C., and Simoni, A.: Physical Interpretation of Rainfall Thresholds or Runoff-Generated Debris Flows, Journal of Geophysical Research: Earth Surface, 125, https://doi.org/10.1029/2019JF005513, 2020.

Boisier, J. P., Alvarez-Garretón, C., Cepeda, J., Osses, A., Vásquez, N., and Rondanelli, R.: CR2MET: A high-resolution precipitation and temperature dataset for hydroclimatic research in Chile, p. 19739, 2018.

Bozkurt, D., Rondanelli, R., Garreaud, R., and Arriagada, A.: Impact of Warmer Eastern Tropical Pacific SST on the March 2015 Atacama Floods, Mon. Weather Rev., 144, 4441–4460, 2016.

Börgel, R.: Geomorfología, Instituto Geográfico Militar (IGM), Santiago, Chile, 1983.

DeWalle, D. R. and Rango, A.: Remote sensing of the snowpack, pp. 118–145, Cambridge University Press, https://doi.org/10.1017/cbo9780511535673.006, 2008.

Falvey, M. and Garreaud, R.: Moisture variability over the South American Altiplano during the SALLJEX observing season, Journal of Geophysical Research: Atmospheres, 110, D22 105, https://doi.org/10.1029/2005JD006152, 2005.

Farr, T. G., Rosen, P. A., Caro, E., Crippen, R., Duren, R., Hensley, S., Kobrick, M., Paller, M., Rodriguez, E., Roth, L., Seal, D., Shaffer, S., Shimada, J., Umland, J., Werner, M., Oskin, M., Burbank, D., and Alsdorf, D.: The Shuttle Radar Topography Mission, Reviews of Geophysics, 45, 2005RG000 183, https://doi.org/10.1029/2005RG000183, 2007.

Fuenzalida, H. A., Sánchez, R., and Garreaud, R. D.: A climatology of cutoff lows in the Southern Hemisphere, J. Geophys. Res. D: Atmos., 110, 2005.

Gafurov, A. and Bárdossy, A.: Snow cover data derived from MODIS for water balance applications, https://doi.org/10.5194/hessd-6-791-2009, 2009.

Garcés, A., Zegers, G., Cabré, A., Aguilar, G., Tamburrino, A., and Montserrat, S.: A modeling methodology to study the tributary-junction alluvial fan connectivity during a debris flow event, Natural Hazards and Earth System Sciences, 22, 377–393, https://doi.org/10.5194/nhess-22-377-2022, 2022.

Garreaud, R.: Estimación de la Línea de Nieve en Cuencas Andinas de Chile Central, Revista de la Sociedad Chilena de Ingeniería Hidráulica, 7, 21–32, 1992.

Garreaud, R.: Warm Winter Storms in Central Chile, Journal of Hydrometeorology, 14, 1515 – 1534, https://doi.org/10.1175/JHM-D-12-0135.1, 2013.

Garreaud, R., Boisier, J. P., Rondanelli, R., Montecinos, A., Sepúlveda, H. H., and Veloso-Aguila, D.: The 2010–2015 megadrought in Central Chile: Impacts on regional hydroclimate and vegetation, Hydrology and Earth System Sciences Discussions, https://doi.org/https://doi.org/10.5194/hess-2017-191, 2020.

Garreaud, R. D.: The Andes climate and weather, Advances in Geosciences, 22, 3–11, https://doi.org/10.5194/adgeo-22-3-2009, 2009.

https://doi.org/10.5194/essd-2026-18
Preprint. Discussion started: 27 March 2026

Hall, D. K. and Riggs, G. A.: MODIS/Aqua Snow Cover Daily L3 Global 500m SIN Grid, Version 61, https://doi.org/10.5067/MODIS/MYD10A1.061, 2021a.

Hall, D. K. and Riggs, G. A.: MODIS/Terra Snow Cover Daily L3 Global 500m SIN Grid, Version 61, https://doi.org/10.5067/MODIS/MOD10A1.061, 2021b.

Hall, D. K., Riggs, G. A., Salomonson, V. V., DiGirolamo, N. E., and Bayr, K. J.: MODIS snow-cover products, Remote Sensing of Environment, 83, 181–194, https://doi.org/10.1016/S0034-4257(02)00095-0, 2002.

Hersbach, H., Bell, B., Berrisford, P., Hirahara, S., Horányi, A., Muñoz-Sabater, J., Nicolas, J., Peubey, C., Radu, R., Schepers, D., Simmons, A., Soci, C., Abdalla, S., Abellan, X., Balsamo, G., Bechtold, P., Biavati, G., Bidlot, J., Bonavita, M., De Chiara, G., Dahlgren, P., Dee, D., Diamantakis, M., Dragani, R., Flemming, J., Forbes, R., Fuentes, M., Geer, A., Haimberger, L., Healy, S., Hogan, R. J., Hólm, E., Janisková, M., Keeley, S., Laloyaux, P., Lopez, P., Lupu, C., Radnoti, G., de Rosnay, P., Rozum, I., Vamborg, F., Villaume, S., and Thépaut, J.-N.: The ERA5 global reanalysis, Quart. J. Roy. Meteor. Soc., 146, 1999–2049, 2020.

JICA: Technical Standards and Guidelines for Planning and Design of Sabo Structures, 2010.

Krajčí, P., Holko, L., Perdigão, R. A. P., and Parajka, J.: Estimation of regional snowline elevation (RSLE) from MODIS images for seasonally snow covered mountain basins, Journal of Hydrology, 519, 1769–1778, https://doi.org/10.1016/j.jhydrol.2014.08.064, 2014.

Matus, F., Paredes, M., Garcés, A., Pinto, D., Lagos-Zúñiga, M., Montserrat, S., and Advanced Mining Technology Center: Comprehensive Catalog of Extreme Precipitation Events in Northern-Central Chile (17.5°S–30°S), https://doi.org/10.5281/ZENODO.14342936, 2025a.

Matus, F., Rondanelli, R., Rutllant, J., and Henderson, S.: Mechanisms for the influence of the Madden–Julian Oscillation on precipitation in Southwestern South America, Journal of Geophysical Research: Atmospheres, 130, e2024JD041 935, https://doi.org/10.1029/2024JD041935, 2025b.

McPhee, J., MacDonell, S., and Casassa, G.: Snow cover and glaciers, Water resources of Chile, pp. 129–151, 2021.

Mo, K. C. and Higgins, R. W.: The Pacific-South American modes and tropical convection during the Southern Hemisphere winter, Monthly Weather Review, 126, 1581–1596, 1998.

Montserrat, S., Aguilar, G., Garcés, A., Lagos-Zúñiga, M., Paredes, M., Pinto, D., Jerez, C., Villela, B., Matus, F., Contreras, T., and Iturra, D.: Guía metodológica para el diagnóstico y cálculo de la amenaza aluvional presente y futura *(Methodological guide for the diagnosis and calculation of present and future debris-flow hazard)*, Advanced Mining Technology Center, Universidad de Chile, Santiago, Chile, 1st edition edn., 2025.

Nikolopoulos, E. I., Destro, E., Maggioni, V., Marra, F., and Borga, M.: Satellite rainfall estimates for debris flow prediction: An evaluation based on rainfall accumulation-duration thresholds, Journal of Hydrometeorology, 18, 2207–2214, https://doi.org/10.1175/JHM-D-17-0052.1, 2017.

Ortega, C., Vargas, G., Rojas, M., Rutllant, J. A., Munoz, P., Lange, C. B., Pantoja, S., Dezileau, L., and Ortlieb, L.: Extreme ENSO-driven torrential rainfalls at the southern edge of the Atacama Desert during the Late Holocene and their projection into the 21th century, Global and Planetary Change, 175, 226–237, https://doi.org/10.1016/j.gloplacha.2019.02.011, 2019.

Romero, J. E., Vergara-Pinto, F., Aguilar, G., Garcés, A., and Montserrat, S.: Triggering factors, behavior, and social impact of the January 2021 hail-debris flows at the Central Valley of Chile, Landslides, 19, 865–883, 2022.

Rondanelli, R.: Cutoff Lows Over Southwestern South America, in: Oxford Research Encyclopedia of Climate Science, 2025.

Rondanelli, R., Hatchett, B., Rutllant, J., Bozkurt, D., and Garreaud, R.: Strongest MJO on record triggers extreme Atacama rainfall and warmth in Antarctica, Geophys. Res. Lett., 46, 3482–3491, 2019.

https://doi.org/10.5194/essd-2026-18
Preprint. Discussion started: 27 March 2026

Rutllant, J. A., Matus, F., Rudloff, V., and Rondanelli, R.: The role of atmospheric rivers in rainfall-induced landslides: A study from the Elqui valley, Journal of Arid Environments, 216, 105 016, https://doi.org/https://doi.org/10.1016/j.jaridenv.2023.105016, 2023.

Takahashi, T.: Debris flow: mechanics, prediction and countermeasures, Taylor & Francis, 2014.

Valenzuela, R., Garreaud, R., Vergara, I., Campos, D., Viale, M., and Rondanelli, R.: An extraordinary dry season precipitation event in the subtropical Andes: Drivers, impacts and predictability, Weather and Climate Extremes, 37, 100 472, https://doi.org/https://doi.org/10.1016/j.wace.2022.100472, 2022.

Valenzuela, R. A. and Garreaud, R. D.: Extreme Daily Rainfall in Central-Southern Chile and Its Relationship with Low-Level Horizontal Water Vapor Fluxes, Journal of Hydrometeorology, https://api.semanticscholar.org/CorpusID:198419503, 2019.

Veloso, J. V.: Analysis of an extreme precipitation event in the Atacama desert in January 2020 and its relationship to humidity advection along the Southeast Pacific, Atmó'sfera, https://doi.org/https://doi.org/10.20937/atm.52911, 2020.

Wilcox, A., Escauriaza, C., Agredano, R., Mignot, E., Zuazo, V., Otárola, S., Castro, L., Gironás, J., Cienfuegos, R., and Mao, L.: An integrated analysis of the March 2015 Atacama floods, Geophys. Res. Lett., 2016.

Zegers, G., Mendoza, P. A., Garcés, A., and Montserrat, S.: Sensitivity and identifiability of rheological parameters in debris flow modelling, Natural Hazards and Earth System Sciences, 20, 1919–1930, https://doi.org/10.5194/nhess-20-1919-2020, 2020.

Zhang, S. J., Xu, C. X., Wei, F. Q., Hu, K. H., Xu, H., Zhao, L. Q., and Zhang, G. P.: A physics-based model to derive rainfall intensity-duration threshold for debris flow, Geomorphology, 351, 106 930, https://doi.org/10.1016/j.geomorph.2019.106930, 2020.